

Analytical and Thermal Modeling of High-Speed Machining With Chamfered Tools

Yiğit Karpaz

e-mail: ykarpaz@eden.rutgers.edu

Tuğrul Özel¹

e-mail: ozel@rci.rutgers.edu

Department of Industrial and Systems
Engineering,
Rutgers University,
Piscataway, NJ 08854-80185

High-speed machining offers several advantages such as increased flexibility and productivity for discrete-part manufacturing. However, excessive heat generation and resulting high temperatures on the tool and workpiece surfaces in high-speed machining leads to a shorter tool life and poor part quality, especially if the tool edge geometry and cutting conditions were not selected properly. In this study, analytical and thermal modeling of high-speed machining with chamfered tools in the presence of dead metal zone has been presented to investigate the effects of cutting conditions, heat generation, and resultant temperature distributions at the tool and in the workpiece. An analytical slip-line field model is utilized to investigate the process mechanics and friction at the tool-chip and tool-workpiece interfaces in the presence of the dead metal zone in machining with a negative rake chamfered polycrystalline cubic boron nitride tool. In order to identify friction conditions, a set of orthogonal cutting tests is performed on AISI 4340 steel and chip geometries and cutting forces are measured. Thermal modeling of machining with chamfered tools based on moving band heat source theory, which utilizes the identified friction conditions and stress distributions on the tool-chip and tool-workpiece interfaces, is also formulated and temperature distributions at the tool, cutting zone, and in the workpiece are obtained. These temperature distributions are compared with the results obtained from finite element simulations. The comparison of temperature fields indicates that the proposed model provides reasonable solutions to understand the mechanics of machining with chamfered tools. Models presented here can be further utilized to optimize the tool geometry and cutting conditions for increasing benefits that high-speed machining offers. [DOI: 10.1115/1.2783282]

Keywords: thermal modeling, chamfered tools, friction factor, dead metal zone, high-speed machining, slip line field analysis

1 Introduction

Chamfered tools with negative rake angle, first proposed by Hitomi [1], are generally used to increase edge strength for machining hard materials. The negative rake angle helps trap the work material in front of the chamfered face, which acts as a cutting edge, protects the tool from rapid wear, and increases the strength of the edge. A stable trapped work material zone as shown in Fig. 1 was observed by many researchers, e.g., Kita et al. [2], Hirao et al. [3], Jacobson and Wallen [4], and Zhang et al. [5], when machining steel and often referred to as dead metal zone (DMZ). Early research was mostly experimental and aimed at classifying the types of dead metal zones under different cutting conditions and chamfered tool designs. Dead metal zone differs from built-up-edge (BUE), which is mostly observed in machining softer materials such as aluminum alloys, because it does not disappear with an increased cutting speed [5]. Recently, some analytical models have been proposed to better understand dead metal zone phenomena and predict cutting forces. Zhang et al. [5] proposed a cutting model for chamfered tools by utilizing the minimum energy method. They observed that the dead metal zone is stationary and its presence does not depend on cutting speed and chamfer angle. Ren and Altintas [6] proposed a similar model which utilizes Oxley's [7] predictive machining model. Movaheddy et al. [8] proposed a thermo-mechanical arbitrary Lagrangian

Eulerian finite element formulation to simulate the chip formation process in orthogonal cutting with chamfered tools. In their study, the zone of stagnant material is identified from the velocity profile around the cutting edge. They concluded that chip formation is not affected by the chamfer angle because of the DMZ formed under the chamfer. Long and Huang [9] extended the models previously proposed by Zhang et al. [5] and Ren and Altintas [6] and considered that the inclination of the dead metal zone under chamfer is not equal to the shear angle as assumed in earlier models [5,6]. However they did not study how dead metal zone angle changes under different cutting conditions. Fang [10] extended Lee and Shaffer's model [11] to study the effect of large negative tool rake angle and cutting speed on the tool-chip friction and the shape of stagnation zone and showed that the size of the stagnation zone decreases with increasing cutting speed. Fang [10] assumed that stagnant zone is parallel to workpiece surface and sticking conditions occur on the stagnant zone. Fang and Wu [12] proposed a slip-line model for positive rake angle chamfered tools without dead metal zone formation in front of the chamfer face and validated their model on aluminum alloys. Choudhury et al. [13] studied the effects of chamfer height and chamfer angle on cutting forces and observed that chamfer height and angle mainly affect thrust (feed) force. In a similar study, Zhou et al. [14] observed the influence of chamfer angle on the tool life of polycrystalline cubic boron nitride (PCBN) tools by investigating the relation between cutting forces and tool wear and found the optimum chamfer angle as negative 15 deg for the given cutting condition. Yen et al. [15] studied the effects of various tool edge geometries on chip formation, cutting forces, and process variables by using finite element analysis. For chamfered tools, they

¹Corresponding author.

Contributed by the Manufacturing Engineering Division of ASME for publication in the JOURNAL OF MANUFACTURING SCIENCE AND ENGINEERING. Manuscript received February 27, 2007; final manuscript received August 2, 2007; published online December 7, 2007. Review conducted by William J. Endres.

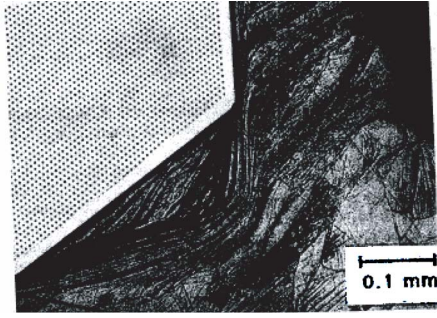


Fig. 1 Dead metal zone when machining austenitic stainless steel with a chamfered tool with 60 deg rake angle at cutting

also observed increasing thrust forces with increasing chamfer angle and increasing thrust and cutting forces with increasing chamfer width.

The objective of this work is to study machining with negative rake angle chamfered tools in the presence of the dead metal zone. Slip-line field analysis will be used to deduce information about the geometry of the dead metal zone and to determine friction factors at the contact interfaces. An analytical thermal model proposed in an earlier study [16–18] will be extended to calculate temperature fields in the tool-chip and tool-workpiece interfaces. An analytical thermal model for machining with chamfered tools will utilize heat intensities generated at the primary deformation zone due to shearing, tool-chip, and dead metal zone-workpiece interfaces due to friction.

Numerous studies on analytical thermal modeling of metal cutting have been undertaken since the pioneering studies of Hahn [19], Jaeger [20] and many others. Recently, Komanduri and Hou [21–23] predicted the temperature distributions in the chip, tool, and workpiece by extending Hahn's solution. An extensive literature survey on thermal modeling in machining can also be found in Komanduri and Hou [21].

2 Slip-Line Modeling for Machining With Chamfered Tools Considering Dead Metal Zone

Modeling of machining by using plasticity theory based slip line field analysis has been a research subject for a long time. Based on Ernst and Merchant's [24] model, Lee and Shaffer [11] applied slip-line field analysis by assuming uniform shear flow stress throughout the slip-line field. Kudo [25] suggested several slip-line models by replacing straight slip lines with curved slip lines in the Lee and Shaffer [11] model. Shi and Ramalingam [26] proposed a slip-line model for worn cutting tools which considered a flank wear land not parallel to the machined surface based on findings of Thomsen et al. [27] which stated that material flow beneath flank wear would not be plastic if flank wear was parallel to the machined surface. Abebe and Appl [28] proposed a slip-line field model for machining with large negative rake angle tools by considering the stagnant metal zone in front of the cutting tool. Waldorf et al. [29] developed a slip-line model to study ploughing and tool wear mechanisms in round edged cutting tools. Fang et al. [30] proposed a universal slip-line model for machining with restricted contact tools. Their proposed model reduces to previously suggested slip-line fields under special cases which therefore can be used to explain the mechanics of machining under various cutting conditions. Fang and Jawahir [31] integrated their universal slip-line field with Oxley's predictive machining theory to investigate the effects of strains, strain rates, and temperatures in machining with grooved tools.

The mechanics of cutting cannot be fully explained by using slip-line field analysis since material characteristics such as strain

hardening, strain rate effects and thermal softening are neglected and non-uniform stress distributions at the interfaces cannot be calculated without violating mass continuity conditions [32]. Recently, Childs [33] compared results of slip-line field analysis with finite element simulations for various materials and concluded that slip-line field analysis provides a legitimate framework for the machining process and yet cannot predict a unique solution for the chip flow.

The slip-line model and its associated hodograph are illustrated in Fig. 2. The chip is assumed to be straight in order to simplify the model. The slip-line angles ζ_1 , ζ_2 , and ζ_3 are the functions of the frictional conditions on the surfaces AD , DF , and FC (Eqs. (2)–(4)), where the tool rake face is in contact with the chip at FC . The shear angle is represented by (ϕ) . The angle formed by bottom surface of the DMZ and the cutting direction is called the DMZ angle (α) .

It is assumed that stagnant and strain hardened DMZ adjacent to the chamfer face acts as part of the cutting edge. Hence the work material flow separates at point D . The work material above point D flows upward into the chip, and the work material under point D flows downward into the workpiece. The inclination of the workpiece material ahead of the tool is also included in the model and shown by prowl angle (ρ) which can be calculated by utilizing the requirement that the height of point E from the uncut workpiece surface should be the same as the height of point D from cut workpiece surface due to velocity continuity as given in Eq. (1) [27].

$$\rho = \sin^{-1} \left(\frac{\sin(\alpha)}{\sqrt{2} \sin(\zeta_1)} \right) \quad (1)$$

In this slip-line model, cut chip thickness (t_c) and cutting forces (F_c and F_t) can be calculated according to uncut chip thickness (t_w), tool-chip friction factor under DMZ ($m_1 = \tau_{AD}/k$), shear angle (ϕ) , dead metal zone angle (α) , and tool geometry (height of the chamfer (h) , rake angles (γ_1) and (γ_2)). The variable τ denotes frictional shear stress and k is the material shear flow stress. The value of friction factor (τ/k) varies between 0 and 1 where a value of zero means no friction occurs, and a value of one means sticking conditions occur. The following expressions can be written from slip-line theory as

$$\zeta_1 = \frac{1}{2} \cos^{-1} \left(\frac{\tau_{AD}}{k} \right), \quad \zeta_2 = \frac{1}{2} \cos^{-1} \left(\frac{\tau_{FD}}{k} \right), \quad \zeta_3 = \frac{1}{2} \cos^{-1} \left(\frac{\tau_{FC}}{k} \right) \quad (2)$$

$$p_E = k \left(1 + 2 \left(\frac{\pi}{4} - \phi - \rho \right) \right) \quad (3)$$

where the expression in the parenthesis in Eq. (3) is equal to slip line field angle θ

$$\theta = \frac{\pi}{4} - \phi - \rho \quad (4)$$

and central fan angle (δ) , the angle $ADF(\Delta)$ can be calculated as

$$\delta = \phi + \zeta_1 - \alpha \quad (5)$$

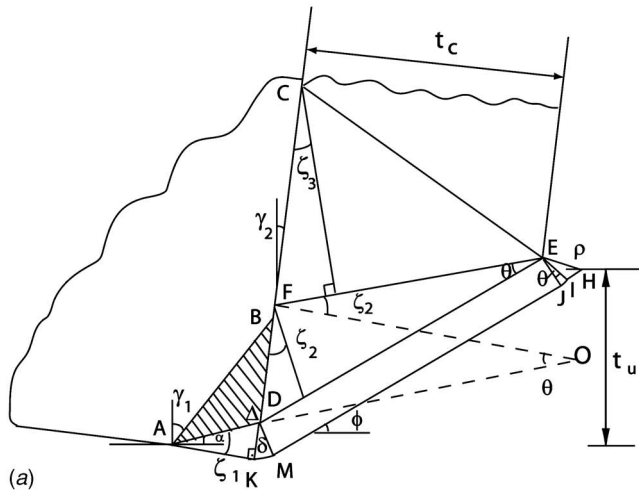
$$\Delta = \frac{\pi}{2} + \frac{\theta}{2} + \zeta_1 + \zeta_2 - \delta \quad (6)$$

In order to simplify the problem, the dead metal zone is assumed to be extending from the rake face which enables us to relate slip line angle ζ_1 to slip line angles ζ_2 and ζ_3 as in Eqs. (7) and (8)

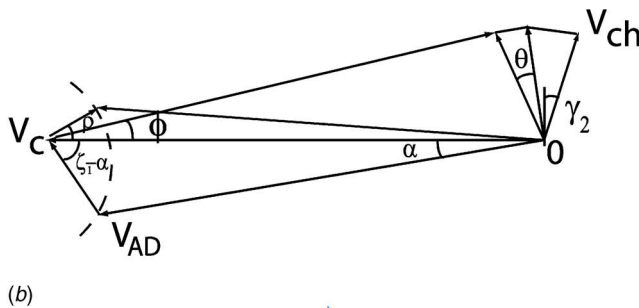
$$\zeta_2 = \zeta_1 + \gamma_2 + \frac{\phi}{2} + \frac{\rho}{2} - \frac{\pi}{8} \quad (7)$$

$$\zeta_3 = \phi - \theta + \gamma_2 \quad (8)$$

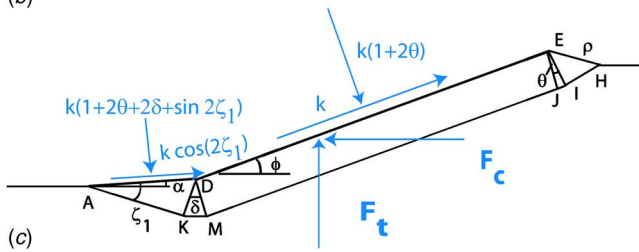
The cut chip thickness (t_c) can be calculated as



(a)



(b)



(c)

Fig. 2 The slip-line model (a); free-body diagram (b); and its hodograph (c)

$$t_c = DE \sin(\pi/2 - \phi - \gamma_2) \quad (9)$$

where

$$DE = \frac{t_u}{\sin(\phi)} \quad (10)$$

It should be noted that absolute values of negative chamfer and rake angles are used in the above given expressions. In an admissible slip-line field, central fan angle (δ), the angle ADF (Δ) (Eqs. (5) and (6)) should be equal to or greater than zero. The free-body diagram of the forces on the primary shear zone is given in Fig. 2(b). Hence, the cutting force and thrust force can be written as

$$F_c = kw \{ DE [\cos(\phi) + (1 + 2\theta)\sin(\phi)] + AD [\cos(\alpha)\cos(2\zeta_1) + (1 + 2\theta + 2\delta + \sin(2\zeta_1))\sin(\alpha)] \}$$

$$F_t = kw \{ DE [(1 + 2\theta)\cos(\phi) - \sin(\phi)] + AD [(1 + 2\theta + 2\delta + \sin(2\zeta_1))\cos(\alpha) - \sin(\alpha)\cos(2\zeta_1)] \} \quad (11)$$

where w is the width of cut. The ratio of cutting force to thrust

force (F_c/F_t) can be calculated from Eq. (11) without necessarily knowing shear flow stress (k) at the primary shear zone. In Eq. (11), the first term on the right hand side represents shearing and the second term represents ploughing forces due to DMZ.

Identification of the unknown slip line angle (θ), DMZ angle (α), and friction factors is performed by utilizing orthogonal cutting tests where cutting forces and chip thicknesses are measured for various cutting conditions and matched to those with slip line field calculations by using a MATLAB code. The unknown slip-line angle pair (θ, α) is solved as a set of possible solutions depending on the tolerance value allowed between measured and calculated force (F_c/F_t) and chip ratios (t_c/t_u) as given in Eq. (12) for a known friction factor m_1

$$\Delta E = \sqrt{\left[\left(\frac{F_c}{F_t} \right)_{ex} - \left(\frac{F_c}{F_t} \right)_{calc} \right]^2 + \left[\left(\frac{t_c}{t_u} \right)_{ex} - \left(\frac{t_c}{t_u} \right)_{calc} \right]^2} \leq \text{Tol} \quad (12)$$

It must be noted that there is a range of m_1 values which will satisfy Eq. (12) depending on the selected tolerance value due to the nonunique nature of the slip-line field model adopted. In this work, a tolerance value of 0.001 has been chosen to narrow the range of the m_1 value. Once all of the slip line angles are calculated, the shear flow stress (k) corresponding to that cutting condition can be calculated by using experimentally measured cutting forces.

According to above given slip-line field model, normal stresses at points A, D, F, and C can be calculated. This yields to the stress distributions on the rake face, front, and bottom interfaces of the dead metal zone as shown in Fig. 3(a). Frictional shear stresses (τ_{AD} , τ_{FD} , and τ_{FC}) on AD, FD, and FC, respectively, are calculated from the solved slip-line angles. Normal stresses at point D and F can be calculated by rotating slip lines ED and EF normal to the rake face as in Eq. (13)

$$\sigma_D = P_E + 2k(\phi + \gamma_2), \quad \sigma_F = k[1 + 2(\phi - \theta + \gamma_2)]$$

$$\tau_{AD} = m_1 k, \quad \tau_{DF} = m_2 k, \quad \tau_{FC} = m_3 k \quad (13)$$

where m_2 ($m_2 = \cos(2\zeta_2)$) and m_3 ($m_3 = \cos(2\zeta_3)$) are the friction factors on DF and FC, respectively. The forces acting on the chamfer tool are shown in Fig. 3(b).

Once the slip-line angles are calculated, resultant force (R_{AB}) acting on the chamfer face of the tool can be calculated by subtracting rake face forces from total cutting forces. The point of application (x) of the resultant force can be found by considering the moment equilibrium around point D. In order for the dead metal zone to remain stagnant at AB, the shear stress on AB must be equal to or less than shear flow stress ($\tau_{AB} \leq k$).

3 Experimental Setup and Results

Orthogonal turning of thin webs (2.5–2.8 mm) were performed on annealed AISI 4340 steel using CBN cutting tool inserts (TNG-423) with chamfered edge design (0.1 mm chamfer land, 20 deg chamfer angle) in a rigid CNC turning center as illustrated in Fig. 4. Low content CBN inserts with properties shown in Table 1 were used. The tool holder provided a negative 7 deg rake angle; hence a negative 27 deg angle is formed at the chamfer face. The image of the chamfered edge preparation of the CBN insert taken by field emission scanning electron microscopy (FESEM) is given in Fig. 5. In the experiments straight edges of triangular inserts were used (see Fig. 4). Forces were measured with a Kistler turret type force dynamometer, a PC-based DAQ system, and Kistler DYNOWARE software, and cut chip thicknesses were measured by using a toolmaker's microscope.

The experiments were conducted under various combinations of three different uncut chip thickness values (0.1 mm, 0.15 mm

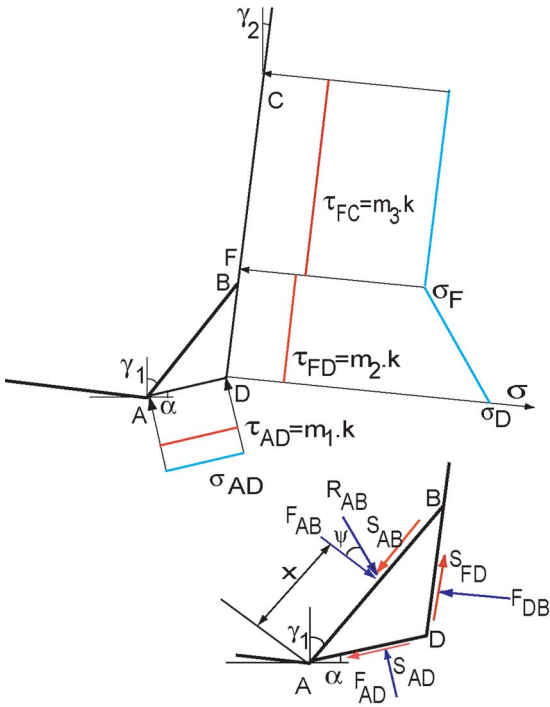


Fig. 3 (a) Normal and shear stress distribution on the chamfered tool; and (b) force equilibrium at the chamfer face

and 0.18 mm) and two different cutting speeds (125 m/min, and 175 m/min). Measured and calculated force ratios and chip thickness values are shown in Fig. 6.

The SEM images of the chips produced under various cutting conditions are shown in Fig. 7. For cutting speed $V=125$ m/min continuous chips were obtained for all uncut chip thickness values. When cutting speed was increased, the formation of serrated chips was observed. Chip thickness is measured as an average for the serrated types of chips. According to experimental results (see Fig. 6): (a) force ratio decreases as uncut chip thickness decreases; (b) force ratio increases as cutting speed increases; and (c) cut chip thickness decreases as cutting speed increases, which

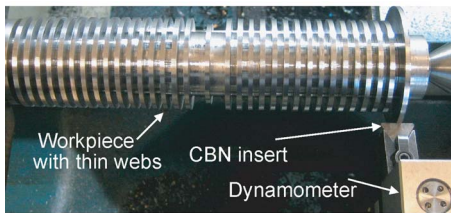


Fig. 4 Experimental setup for orthogonal turning

Table 1 Properties of CBN tool material

Properties	Low content CBN
Density (ρ) (kg m^{-3})	4280
Elasticity (E) (GPa)	587
Poisson's ratio (ν)	0.13
Conductivity (k) ($\text{W m}^{-1} \text{K}^{-1}$)	44
Specific heat (c) ($\text{J Kg}^{-1} \text{K}^{-1}$)	750
Expansion (K^{-1})	$4.7 \cdot 10^{-6}$

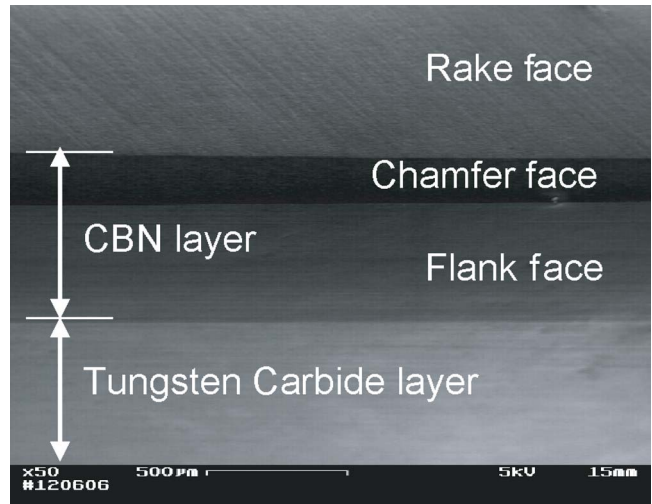


Fig. 5 SEM image of the chamfered insert at 50 times magnification

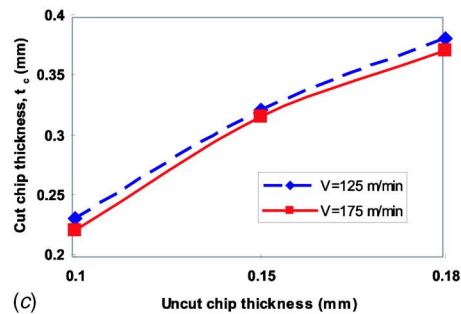
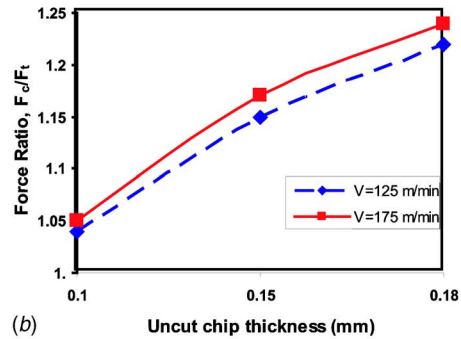
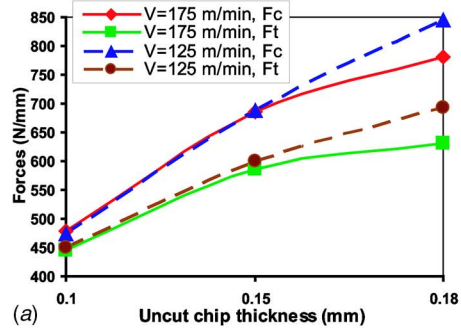


Fig. 6 Measured: (a) forces; (b) force ratio; and (c) cut chip thickness

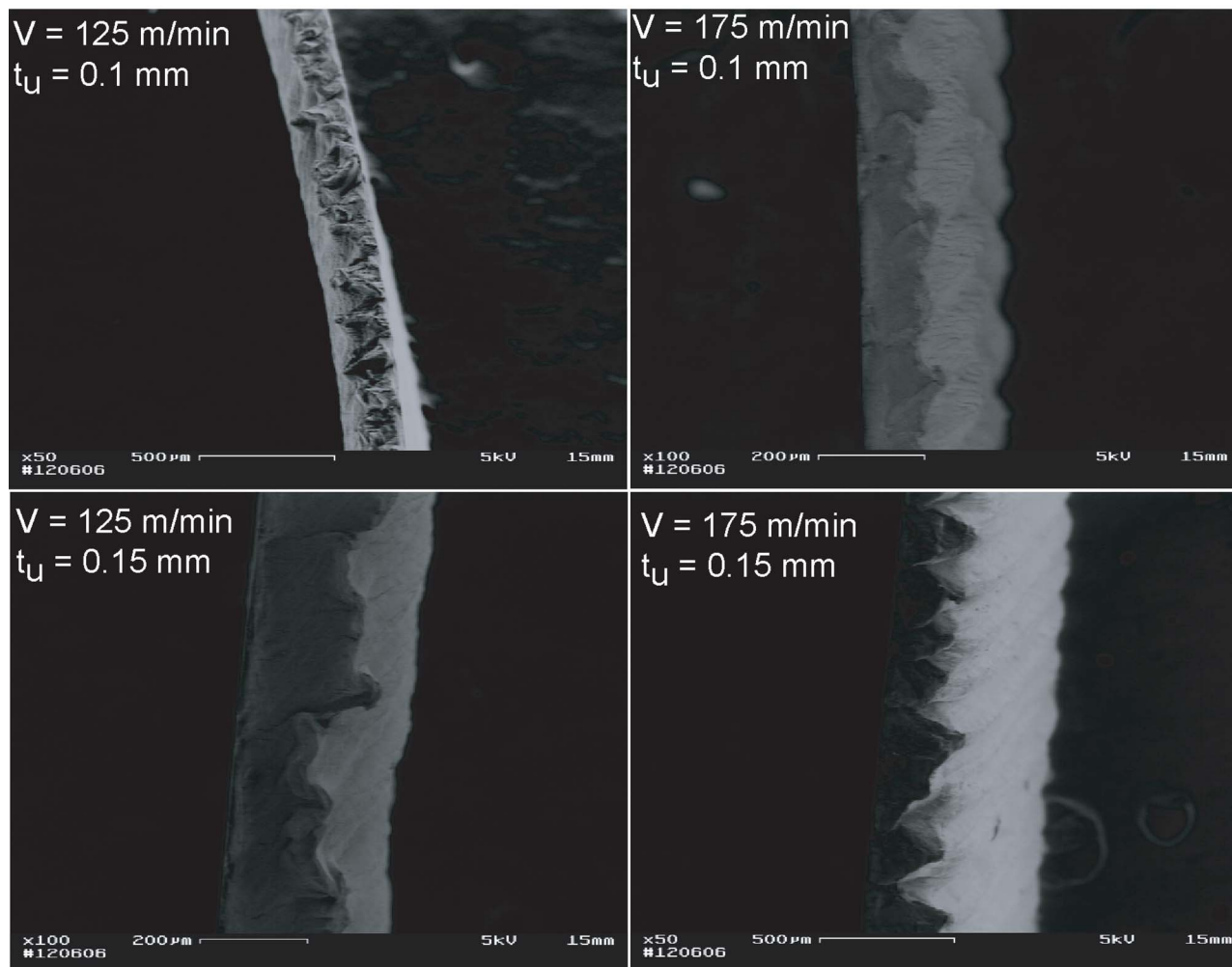


Fig. 7 SEM images of the chips collected during experiments

are in agreement with general orthogonal machining observations.

4 Identification of Slip-Line Angles and Friction Factors

The slip-line field angle (θ) and DMZ angle (α) are identified for various cutting conditions by using measured force and chip thickness ratios given in Fig. 6. A range of friction factors (m_1) which satisfies the tolerance term given in Eq. (14) is obtained. The number of solutions can be further reduced by decreasing the tolerance value in Eq. (14). However, a wide range solution allows us to observe the effects of friction factor under DMZ (m_1) on the slip-line angles.

These identified slip-line angles are shown in Figs. 8(a)–8(c) for the cutting speed of $V=125$ m/min. From the identified slip-line angles, the following observations can be made:

- As friction factor under DMZ (m_1) increases, DMZ angle (α) decreases and slip-line field angle (θ) increases. This implies that friction factor under the DMZ affects the shape of the primary deformation zone;
- Increased friction factor under DMZ (m_1) and resulting decreased DMZ angle (α) change primarily the thrust force. It must be noted that the ratio of cutting force to thrust force remains the same for all possible slip-line field angles. Therefore, this implies that the friction conditions on the front of dead metal zone (along DF) and rake face (along

BC) should increase in response to increasing friction under DMZ in order to maintain the same resultant force ratio;

- DMZ angle (α) decreases as uncut chip thickness increases and increases as cutting speed increases; and
- Slip-line field angle (θ) decreases with increasing cutting speed and decreases with increasing uncut chip thickness.

Friction factors calculated on the front boundary of the dead metal zone DF (m_2) and on the rake face (m_3) are given in Fig. 9 for various cutting conditions. While friction factors on DF (m_2) and rake face (m_3) are significantly different (25% lower on DF) than each other, they are not so sensitive (less than 5%) to the changes in experimental cutting conditions used in this study. These friction factors slightly decrease with increasing uncut chip thickness and increase with increasing cutting speed.

The temperatures at the dead metal zone are expected to increase with increasing uncut chip thickness since the decreasing dead metal zone angle will result in higher heat intensity at the bottom surface of the DMZ. This will also result in temperature rise and decreasing friction factor on the front of the DMZ. Due to the thermal softening property of steels, machining under these conditions becomes more favorable. This further justifies usage of chamfered tools in roughing operations where large uncut chip thicknesses are taken.

The distribution of normal stresses along DC extended from the front end of the DMZ to the rake face of the chamfered tool is shown in Fig 10. Normal stress at point D is found to be around

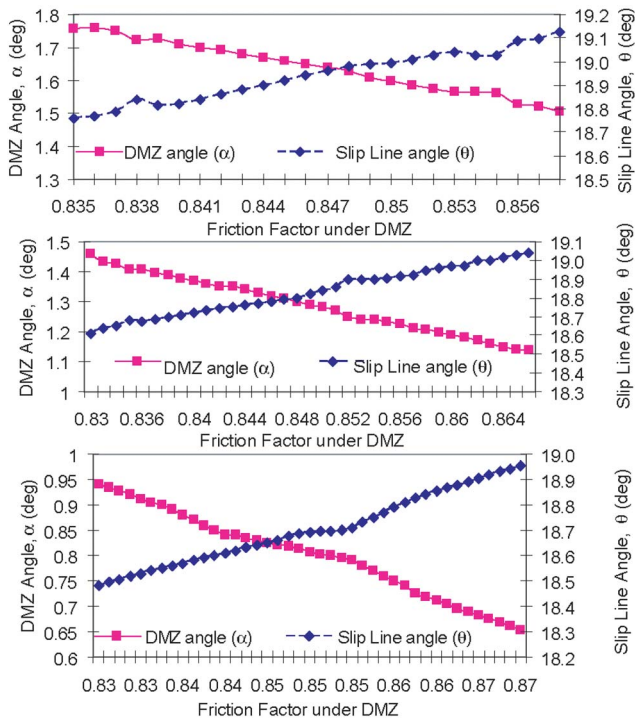


Fig. 8 Identified dead metal zone angle (α) and slip line field angle (θ) for $V=125$ m/min: (a) $t_u=0.1$ mm; (b) $t_u=0.15$ mm, and (c) $t_u=0.18$ mm

2.5 or 3 times the shear flow stress of work material, which is in agreement with observation by Childs [33]. Due to increased chip load, normal stresses applied to the rake face increase with the increase in uncut chip thickness as expected. Shear stress applied to the rake face decreases due to decreasing friction factor with increasing uncut chip thickness (Fig. 9).

The stress distributions can be further utilized to calculate the force partition on the chamfered and rake faces of the cutting tool. As uncut chip thickness increase 80% from 0.1 mm/rev to 0.18 mm/rev, the percentage of the resultant force exerted on the chamfered face decreases from 45% to 31%, and the percentage of the resultant force exerted on the rake face increases from 55% to 69%. Figure 11 illustrates the changes in percentage of resultant force on the chamfer face. This indicates that the slip-line field model can be beneficial in investigating the

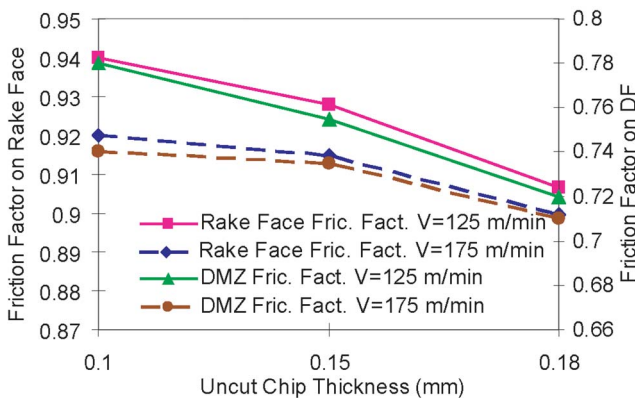


Fig. 9 Variation of rake face friction factor with uncut chip thickness and cutting speed

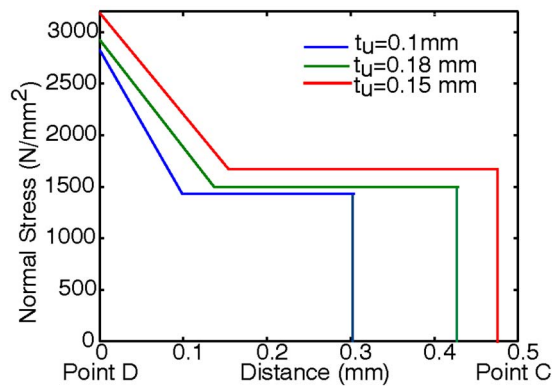


Fig. 10 Distribution of normal stresses for $V=125$ m/min on the rake face of the tool

effects of the chamfer angle and chamfer height on the mechanics of cutting and proper selection of cutting tool for a given cutting condition.

In order to be able to investigate the effects of cutting conditions on tool temperature distributions, an analytical thermal model is proposed for orthogonal machining with chamfered tools. The proposed analytical thermal model utilizes identified friction factors, velocities, shear angle, length, of primary shear zone, DMZ geometry, tool-chip contact length, and stress distributions at the interfaces to calculate the heat intensities and obtain temperature distributions in the tool and cutting zone.

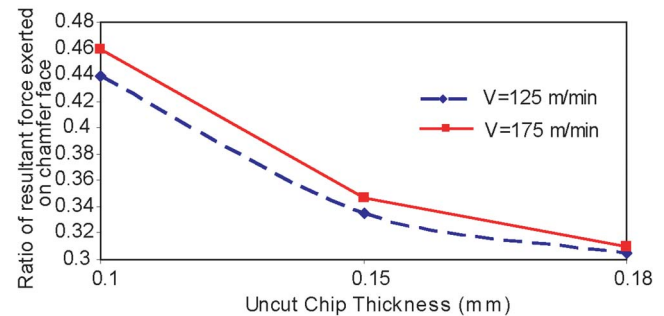


Fig. 11 Percentage of resultant force exerted on the chamfer face

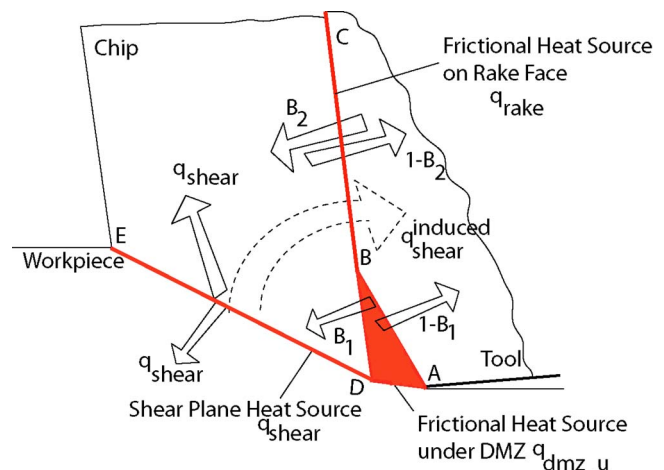


Fig. 12 Heat sources in thermal modeling of orthogonal cutting with a chamfered tool

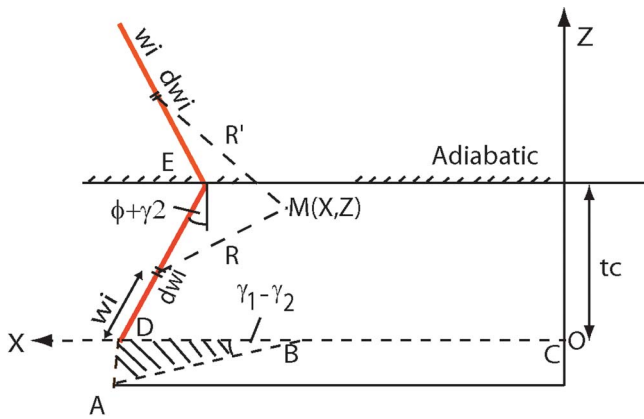


Fig. 13 Shear plane heat source

According to results given in Fig. 11, at uncut chip thickness of 0.1 mm, the load partition between chamfer and rake faces is found to be 46% and 54%, respectively. It is seen that an uncut chip thickness to chamfer height ratio of 1 results in around 45% chamfer load. If this ratio is increased to 1.5 and 1.8, then the percentage of load taken by the chamfer reduces to 35% and 30%, respectively. This supports the industrial common practice of selecting an uncut chip thickness (feed) to chamfer height (land) as 1.

5 Thermal Modeling of Chamfered Tools for Orthogonal Machining

The heat sources considered in the analytical thermal model and the regions affected by these heat sources are shown in Fig. 12. A shear plane heat source is considered as a uniform oblique moving band heat source. The heat intensity of the frictional heat source is modeled as a nonuniform moving band heat source on the chip side and a stationary heat source on the tool side. The frictional heat intensity on *BD* is neglected considering the low heat intensity at that region as a result of low chip velocity. Frictional heat source under dead metal zone is also modeled as a moving band heat source. This heat source is considered to heat up the workpiece and dead metal zone. In order to satisfy continuity conditions, the heating effect of the shear plane heat source on the tool will be modeled as an induced stationary heat source on the chamfered and rake faces.

An analytical thermal model yields steady-state temperatures at the cutting zone in a very short amount of time. It allows the investigation of heat partitioning between chip and tool. In the analytical thermal model, it is assumed that: (i) The temperature distributions on the interfaces are the same, which enables the

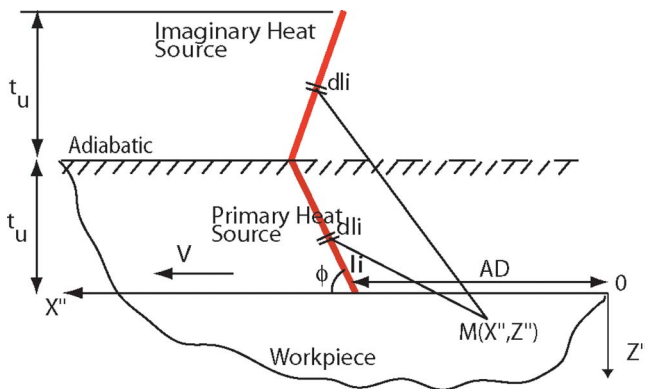


Fig. 14 Thermal modeling of primary heat source on the workpiece side

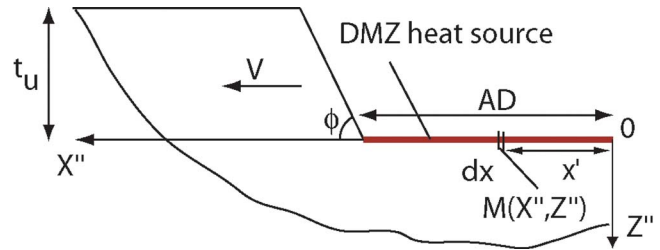


Fig. 15 Thermal modeling of DMZ heat source on the workpiece side

calculation of the heat partition ratios on the rake and chamfer faces; (ii) The upper surface of the chip, the uncut surface of the workpiece, and the tool side of the tool-chip interface are considered adiabatic; (iii) The temperature distributions are in steady state; (iv) Heat loss along the tool-chip interface is omitted and it is assumed that all the deformation energy in the primary shear zone is converted into heat energy; and (v) All the heat sources are plane heat sources.

5.1 Modeling of Temperature Rise in the Chip Due to Shear Plane Heat Source. The analytical modeling of steady-state temperature in metal cutting presented by Hahn [19] was based on the heat source method of Jaeger [20]. Komanduri and Hou [21,23] modified Hahn's infinite medium oblique band heat source solution and obtained a semi-infinite medium oblique band heat source solution by considering the upper surface of the chip as adiabatic and adding an appropriate image heat source as shown in Fig. 13. The coordinate system (*X, Z*) is located at point *O*. The temperature rise at any point can be calculated with Eq. (14).

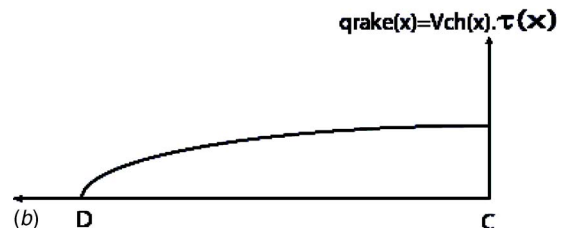
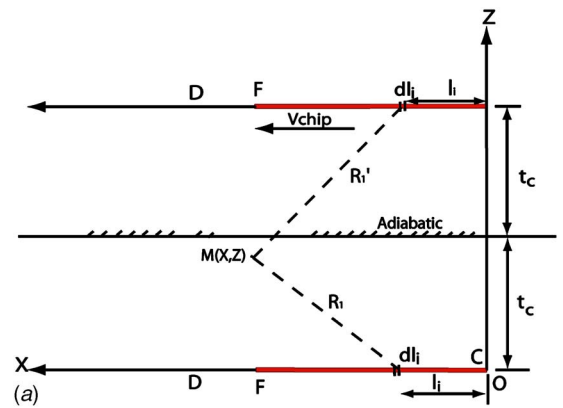


Fig. 16 (a) Frictional heat source along tool chip interface; and (b) nonuniform heat intensity

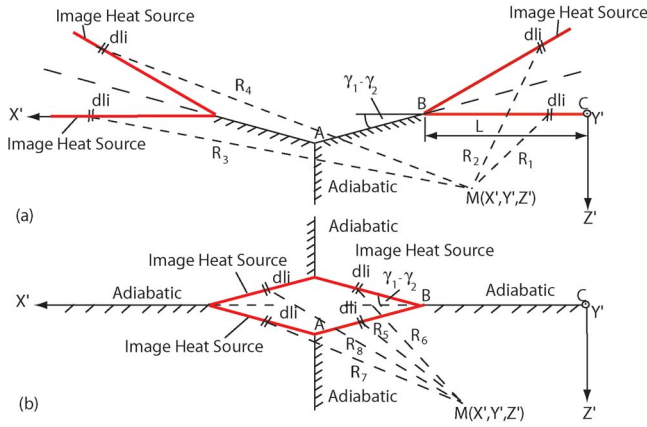


Fig. 17 Thermal modeling on the tool side: (a) rake face; and (b) chamfer face

$$T_{M_{\text{chip-shear}}}(X, Z) = \frac{q_{\text{shear}}}{2\pi\lambda_c} \int_{w_i=0}^{\overline{DE}} e^{-(X-X_i)V_{\text{ch}}/2a_c} \times \left\{ K_0 \left[\frac{V_{\text{ch}}}{2a_c} \sqrt{(X-X_i)^2 + (Z-Z_i)^2} \right] + K_0 \left[\frac{V_{\text{ch}}}{2a_c} \sqrt{(X-X_i)^2 + (2 \cdot t_c - Z_i - Z)^2} \right] \right\} dw_i$$

$$X_i = \overline{DC} - w_i \sin(\phi + \gamma_2), \quad Z_i = w_i \cos(\phi + \gamma_2), \quad q_{\text{shear}} = k \cdot V_{\text{shear}} \quad (14)$$

By using Eq. (14), temperature rise at any point in the chip due to shear plane heat source can be calculated.

As for the workpiece side of the thermal modeling, the primary heat source is modeled again as an oblique moving band heat source which moves with cutting velocity as given in Komanduri and Hou [21,23]. The uncut workpiece surface is considered as adiabatic (see Fig. 14). Assuming the origin of the coordinate system to be at point A, the following expressions can be derived

$$T_{M_{\text{workpiece-shear}}}(X'', Z'') = \frac{q_{\text{shear}}}{2\pi\lambda_c} \int_{l_i=0}^{\overline{DE}} e^{-(X''-l_i \cos \phi - AD)V/2a_c} \times \left\{ K_0 \left[\frac{V}{2a_c} \sqrt{(AD + l_i \cos \phi - X'')^2 + (Z'' + l_i \sin \phi)^2} \right] + K_0 \left[\frac{V}{2a_c} \sqrt{(AD + l_i \cos \phi - X'')^2 + (2t_u + Z'' - l_i \sin \phi)^2} \right] \right\} dl_i \quad (15)$$

The frictional heat source under the dead metal zone due to rubbing is modeled as a band heat source moving along the tool-workpiece surface with cutting velocity as in Carslaw and Jaeger [34]. Since the heat source does not move obliquely it coincides with its imaginary heat source as shown in Fig. 15.

The temperature rise at any point in the workpiece due to DMZ heat source can be written as

$$T_{M_{\text{dmz}}}(X'', Z'') = \frac{q_{\text{dmz},u}}{\pi\lambda_c} \int_0^{\overline{AD}} (1-\psi)e^{(X''-x'')V_{\text{dmz}}/2a_c} \times \left[K_0 \left(\frac{V_{\text{dmz}}}{2a_c} \sqrt{(X''-x'')^2 + Z''^2} \right) \right] dx'' \quad (16)$$

Table 2 Heat intensities at various locations around cutting zone

Cutting speed cm/min	Uncut chip thickness (mm)	q_{shear} (J/mm ² s)	q_{rake} (J/mm ² s)	$q_{\text{DMZ},u}$ (J/mm ² s)
V=125	0.1	2500	884	1680
V=175	0.1	3730	1363	2590

5.2 Modeling of Temperature Rise in the Chip Due to Frictional Heat Sources. The effect of frictional heat source along the tool-chip interface on the chip side is modeled as a nonuniform moving band heat source and the temperature rise at any point in the chip due to these heat sources can be calculated with Eq. (17). The tool rake face and upper surface of the chip are considered to be adiabatic as shown in Fig. 16. Since the heat sources are on the boundary, the solution for a semi-infinite medium will be twice that for an infinite medium [21]. The origin of the coordinate system (X, Z) for the moving heat source on the rake face is at point C. The thermal modeling on the rake face is equivalent to one given for sharp tool in [16].

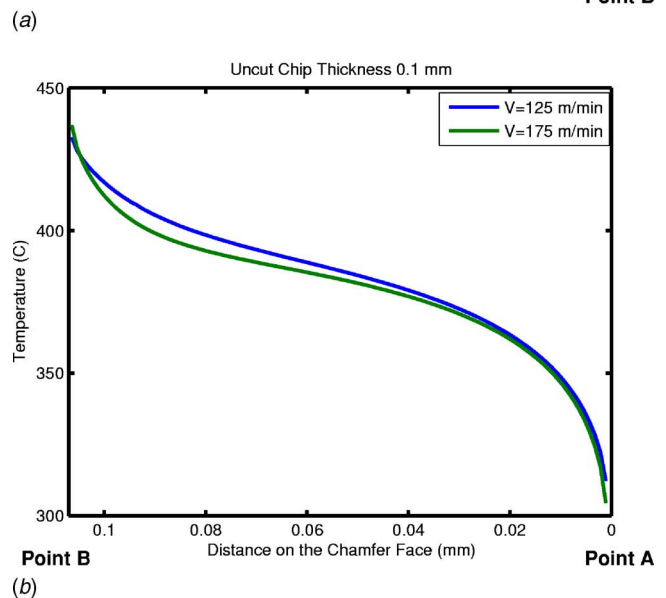
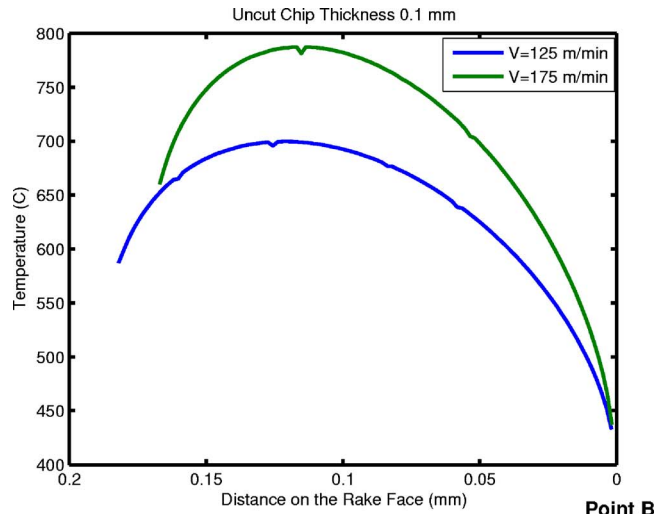


Fig. 18 Temperature distribution at the: (a) rake and (b) chamfer interfaces for $t_u=0.1$ mm

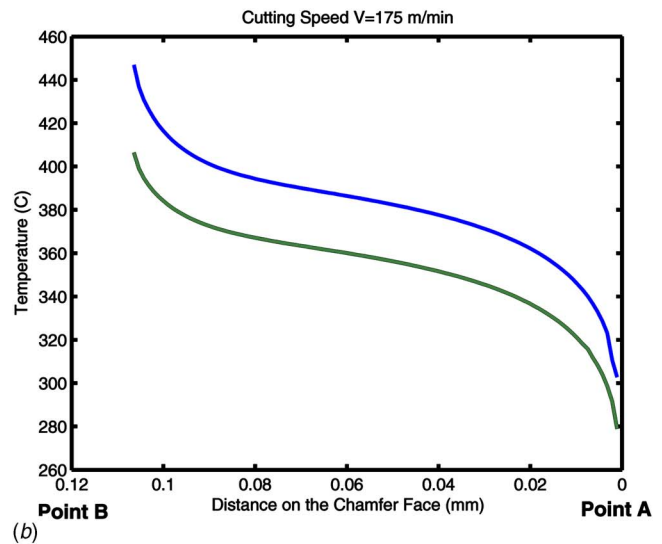
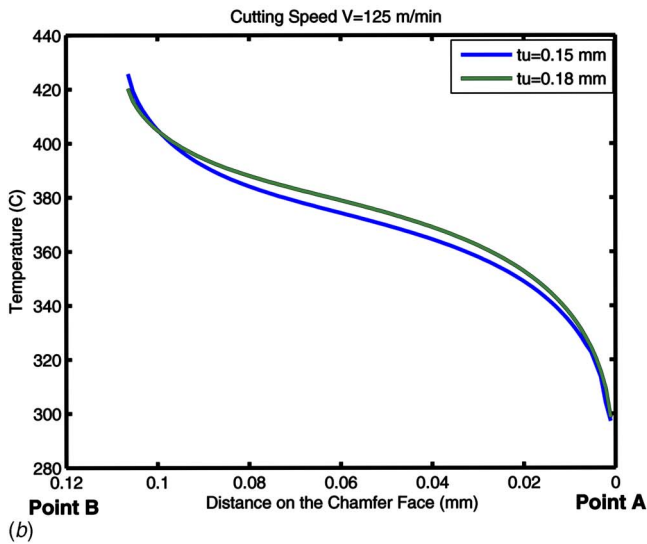
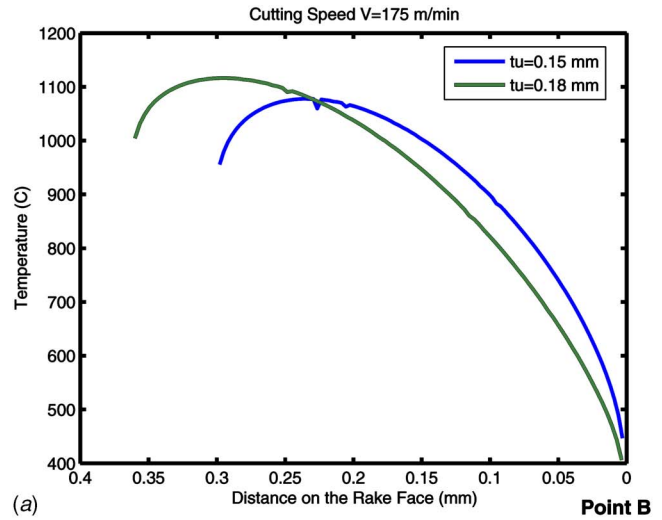
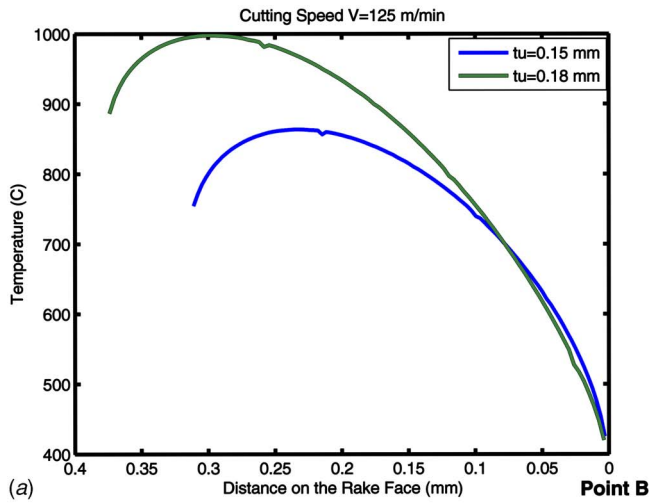


Fig. 19 Temperature distribution along the: (a) rake and (b) chamfer interfaces for $V=125$ m/min and various uncut chip thickness values

Fig. 20 Temperature distribution along the: (a) rake and (b) chamfer interfaces for $V=175$ m/min and various uncut chip thickness values

$$T_{M_{\text{chip-friction}}}(X, Z) = \frac{B_2}{\pi \lambda_c} \int_{l_i=0}^{\overline{CF}} q_{\text{rake}}(l_i) e^{-(X-l_i)V_{\text{ch}}/2a_c} \cdot \left[K_0 \left(R_1 \frac{V_{\text{ch}}}{2a_c} \right) + K_0 \left(R_1' \frac{V_{\text{ch}}}{2a_c} \right) \right] dl_i$$

$$R_1 = \sqrt{(X-l_i)^2 + (Z)^2}$$

$$R_1' = \sqrt{(X-l_i)^2 + (2 \cdot t_c - Z)^2}, \quad q_{\text{rake}}(l_i) = \tau_{CF} V_{\text{ch}}(l_i) \quad (17)$$

where B_2 denotes the heat partition ratio.

5.3 Modeling of Temperature Rise in the Tool Due to Stationary Heat Sources. The tool side of the frictional heat source is modeled as a stationary rectangular heat source on the rake face. The image heat sources are added to satisfy adiabatic boundary conditions on the rake, chamfer, and clearance faces as shown in Fig. 17.

The temperature rise on the tool side can be written with the expressions given in Eq. (18)

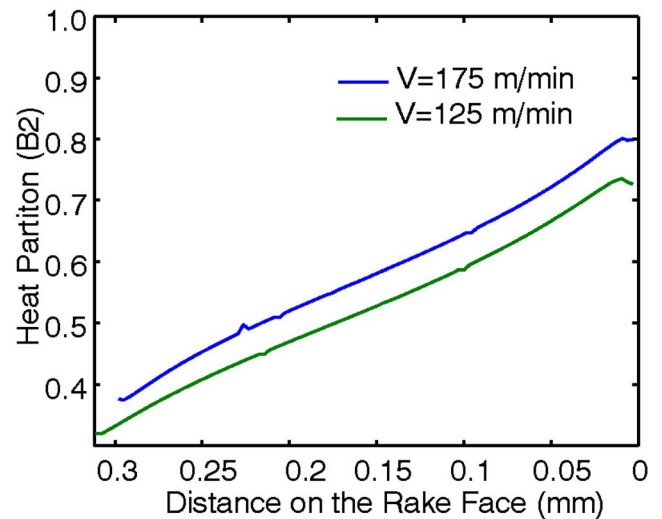


Fig. 21 Heat partition along rake face for $t_u=0.15$ mm

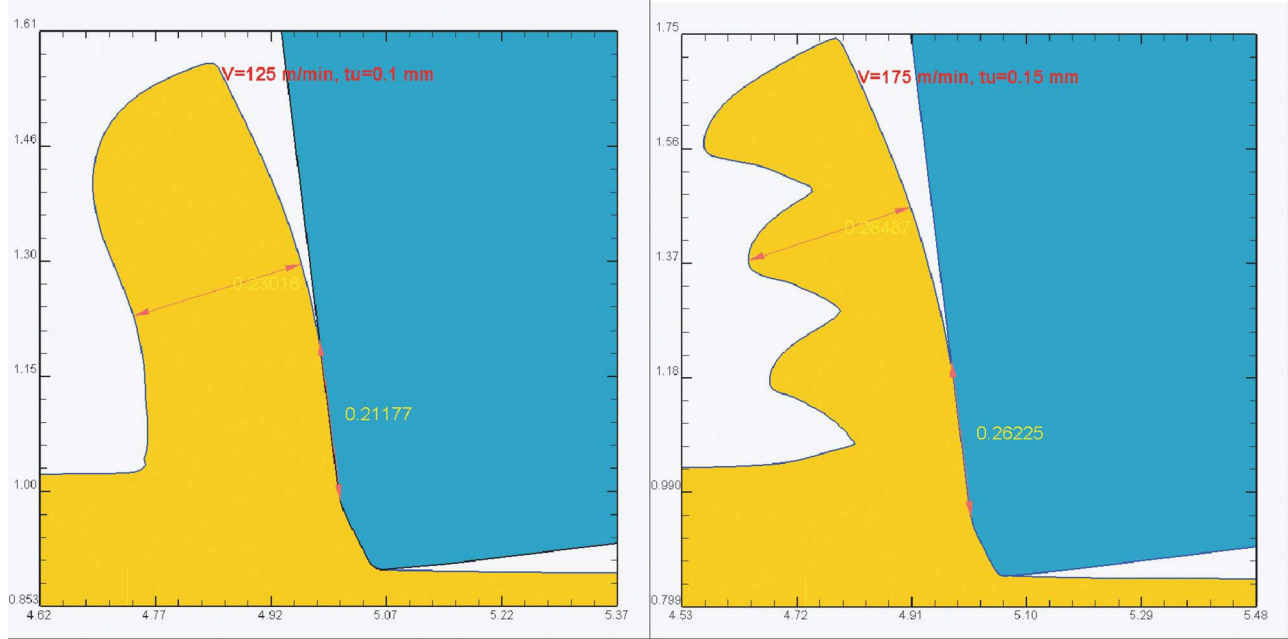


Fig. 22 Simulated chip formation for the cutting conditions of $V=125$ m/min, $t_u=0.1$ mm and $V=175$ m/min, $t_u=0.15$ mm

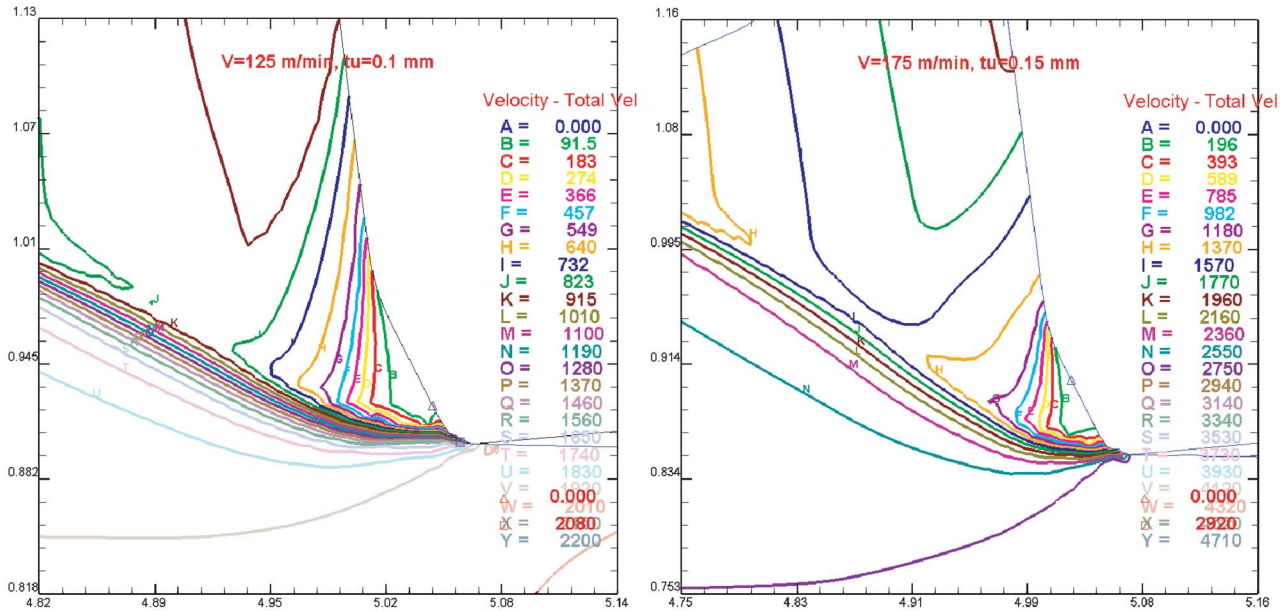


Fig. 23 Velocity field for the cutting conditions of $V=125$ m/min, $t_u=0.1$ mm and $V=175$ m/min, $t_u=0.15$ mm

$$T_{M_{\text{sta-rake}}}(X', Y', Z') = \frac{(1 - B_2)}{4\pi\lambda_t} \left[\int_{-w/2}^{w/2} \int_{l_i=0}^{\overline{BC}} q_{\text{rake}}(l_i) \left(\frac{1}{R_1} + \frac{1}{R_3} \right) dl_i dy_i + \int_{-w/2}^{w/2} \int_{l_i=0}^{\overline{BC}} q_{\text{rake}}(l_i) \left(\frac{1}{R_2} + \frac{1}{R_4} \right) dl_i dy_i \right]$$

$$T_{M_{\text{sta-cham}}}(X', Y', Z') = \frac{(1 - B_1)\psi q_{\text{dmz-u}}}{4\pi\lambda_t} \left[\int_{-w/2}^{w/2} \int_{h_i=0}^{\overline{AB}} \left(\frac{1}{R_5} + \frac{1}{R_7} \right) dh_i dy_i + \int_{-w/2}^{w/2} \int_{h_i=0}^{\overline{AB}} \left(\frac{1}{R_6} + \frac{1}{R_8} \right) dh_i dy_i \right]$$

$$R_1 = \sqrt{(X' - l_i)^2 + Z'^2 + (Y' - y_i)^2}, \quad R_3 = \sqrt{(2\overline{BC} + 2\overline{AB} \cos(\chi) - X' - l_i)^2 + Z'^2 + (Y' - y_i)^2}$$

$$R_2 = \sqrt{(X' - (\overline{BC} - l_i) \cos(2\chi) - \overline{BC})^2 + (Z' + (\overline{BC} - l_i) \sin(2\chi))^2 + (Y' - y_i)^2}$$

$$R_4 = \sqrt{(\overline{BC} + 2\overline{AB} \cos(\chi) + \overline{BC} \cos(2\chi) - l_i \cos(2\chi) - X')^2 + (Z' + (\overline{BC} - l_i) \sin(2\chi))^2 + (Y' - y_i)^2}$$

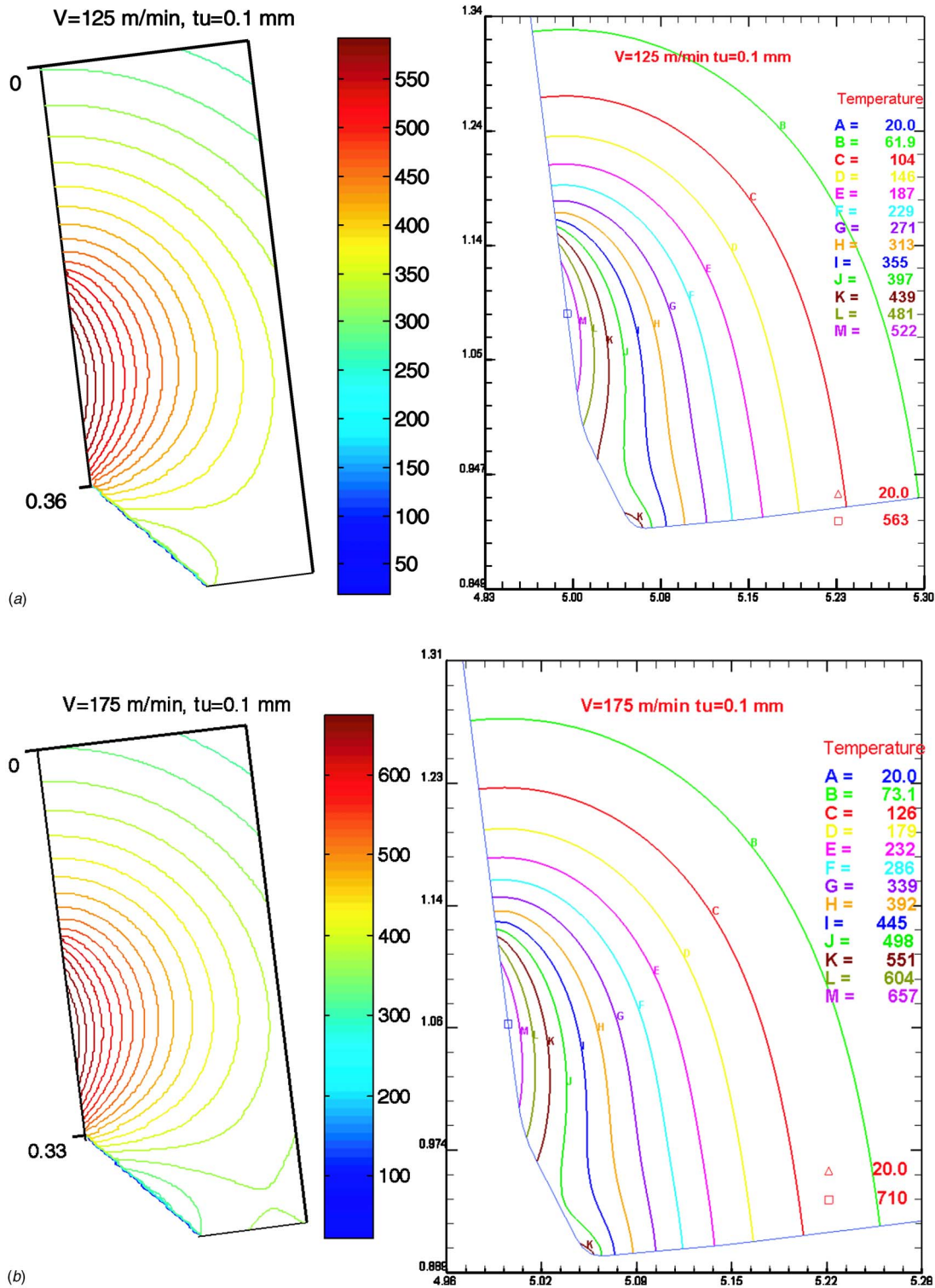


Fig. 24 Isotherms obtained from analytical method for: (a) $V=125$ m/min, $t_u=0.1$ mm; and (b) $V=175$ m/min, $t_u=0.1$ mm (all temperatures are in °C)

$$R_5 = \sqrt{(BC + h_i \cos(\chi) - X')^2 + (Z' - h_i \sin(\chi))^2 + (Y' - y_i)^2}, \quad R_6 = \sqrt{(BC + h_i \cos(\chi) - X')^2 + (Z' + h_i \sin(\chi))^2 + (Y'' - y_i)^2}$$

$$R_7 = \sqrt{(BC + 2AB \cos(\chi) - h_i \cos(\lambda) - X')^2 + (Z' - h_i \sin(\chi))^2 + (Y' - y_i)^2}$$

$$R_8 = \sqrt{(BC + 2AB \cos(\chi) - h_i \cos(\lambda) - X')^2 + (Z' + h_i \sin(\chi))^2 + (Y' - y_i)^2}$$

$$\chi = \gamma_1 - \gamma_2, \quad q_{dmz,u} = \tau_{AD} V_{dmz} \quad (18)$$

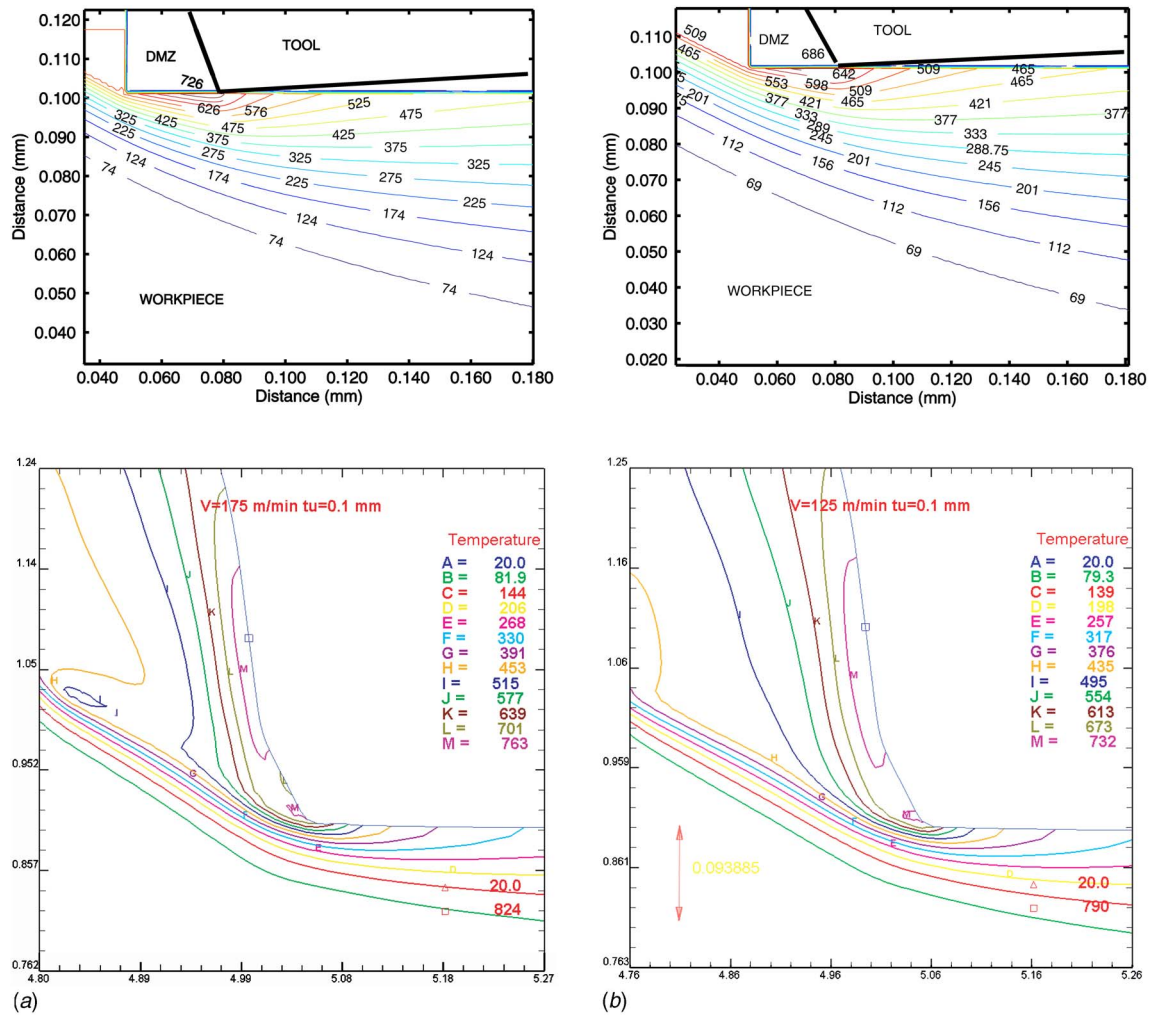


Fig. 25 Temperature distributions in the workpiece: (a) $V=175$ m/min, $t_u=0.1$ mm and (b) $V=125$ m/min, $t_u=0.1$ mm (all temperatures are in $^{\circ}\text{C}$)

It should be noted that if $\gamma_1 - \gamma_2$ in Eq. (18) is taken as zero, the thermal model reduces to the sharp tool thermal model given in [16].

The heating effect of the frictional heat source under the dead metal zone on the chamfer face of the tool is modeled by multiplying the heat intensity ($q_{dmz,u}$) with a heat partition factor (ψ) as shown in Eqs. (16) and (18). Considering most of the heat generated at this heat source will be transferred into the workpiece, the heat partition factor is taken as 0.2 in this study.

The heat partition ratios (B_1) and (B_2) can be found numerically by matching the temperature distributions on the chip and the tool side for both rake and chamfer faces. The thermal equilibrium is represented by Eq. (19)

$$T_{M_{\text{chip-shear}}}(X, 0) + T_{M_{\text{chip-friction}}}(X, 0) = T_{M_{\text{sta-cham}}}(X, 0) + T_{M_{\text{sta-rake}}}(X, 0) + T_{M_{\text{induced}}}(X, 0) \quad (19)$$

The intensity of the induced heat source, heating effect of shear plane heat source in the tool, can be calculated in a similar fashion as explained in [16–18].

6 Results and Model Validation

The solution for the analytical thermal model is performed via computer programs developed in MATLAB. The solution has been performed either by solving the temperature equilibrium given in Eq. (19) numerically along the tool-chip interface in a discrete fashion or simply by solving the equilibrium of the average tem-

peratures in the chip and the tool side. Temperature rise in any point in shear zone and workpiece underneath the dead metal zone can also be calculated from Eqs. (15) and (16). The calculated heat intensities are given in Table 2. The temperature distributions and isotherms obtained from these solutions are given below.

6.1 Temperature Distributions Along the Tool Chamfer and Rake Face

The temperature distributions along the rake and chamfer face are computed under various cutting conditions. Fig. 18 shows the effect of the cutting speed on tool-chip interface temperatures for a given uncut chip thickness. As cutting speed increases, rake face temperatures increase. Temperature distributions along the chamfer face seem to be the same for both cutting speeds.

Increasing the uncut chip thickness also increases the temperatures at the rake face. In Fig. 19, the effect of the increasing uncut chip thickness on the temperature distributions at the interfaces is shown.

Figure 20 shows the temperature distributions along the rake and chamfer interfaces for $V=175$ m/min and different uncut chip thickness values. In Fig. 20(a), increasing uncut chip thickness resulted in only a slight increase in the maximum temperature at the rake face, however slightly lower temperatures on the chamfer face.

It should be noted that when cutting speed increased, lower temperature rises take place at the chamfered face. In order to explain why lower temperatures at the chamfer face are obtained

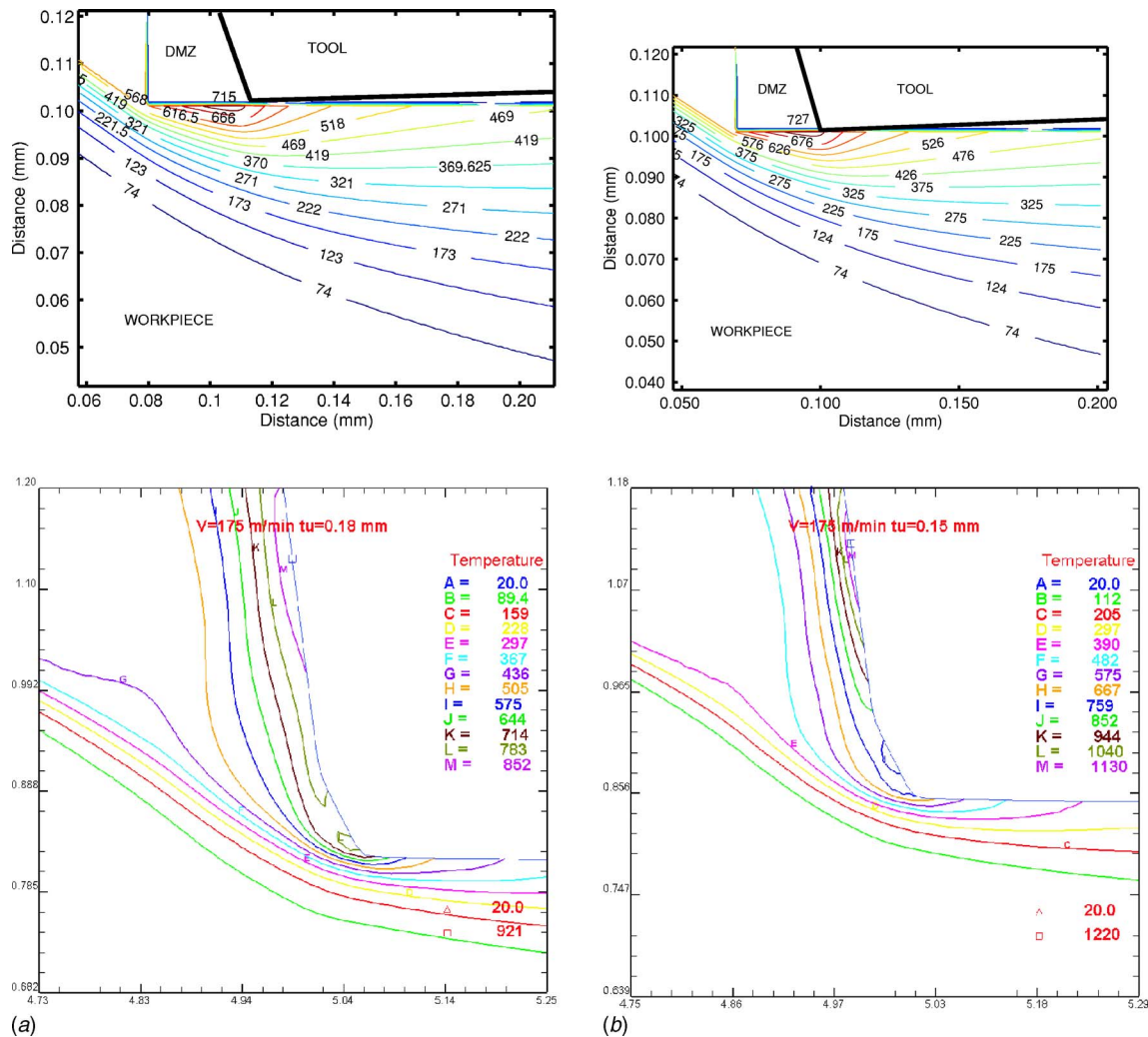


Fig. 26 Temperature distributions in the workpiece: (a) $V=175$ m/min, $t_u=0.18$ mm and (b) $V=175$ m/min, $t_u=0.15$ mm (all temperatures are in °C)

for increasing uncut chip thickness values at higher cutting speeds, the nonuniform heat partitions along the rake face are calculated as given in Fig. 21.

It is clear from Fig. 21 that the local heat partition along the rake face increases. It indicates a steady temperature rise in the chip as the chip travels along the rake face and leaves the contact at a higher temperature. Most of the heat energy is carried away within the chips when cutting speed increases, which is the original premise of high-speed cutting. Hence, this observation is a self-evident validation of the proposed thermal model and its solution.

6.2 Comparison of Calculated Temperature Fields With FEA. In order to compare the temperature distributions computed using the analytical thermal model for machining with chamfered tools, finite element (FE) simulations were performed under the same cutting conditions using commercial software DEFORM-2D®. Identified rake face friction factors through slip-line field analysis are used in these simulations. Workpiece is modeled as rigid, perfectly plastic material. Johnson-Cook (JC) [35] material model parameters for AISI 4340 steel are adapted from Gray et al. [36]. In their study, Gray et al. investigated the JC parameters for various materials by using the split Hopkinson bar test and calculated most suitable JC parameters for AISI 4340 steel as $A = 1504$ MPa, $B = 569$ MPa, $n = 0.22$, $C = 0.003$, and $m = 0.9$. The Cockcroft-Latham [37] damage model is implemented in the finite element model (FEM) to simulate serrated chip formation. Its

critical damage value is fine tuned by observing the chip shapes and comparing them with scanning electron microscope (SEM) images. This critical damage value was found to be around 290 MPa for annealed AISI 4340 steel. Simulated chip thicknesses are found to be in agreement with the measured values as shown in Fig. 22.

A stagnant metal zone can be seen in FE simulations, when velocity field is plotted as shown in Fig. 23. In this figure, the triangular area adjacent to the chamfer face with a very low velocity value may indicate the possible dead metal zone formation.

The temperature fields in the tool are calculated for two different cutting conditions and compared with FE simulations as shown in Fig. 24. The temperature fields in the shear zone and in the workpiece are also calculated for six different cutting conditions as given in Figs. 25–27. These temperature fields reveal the temperature rise effects of the deformation zones that the workpiece undergoes in the primary shear zone and underneath the DMZ. According to these isotherms, the maximum temperature location in the workpiece is seen to be at the tip of the chamfer face in both analytical thermal calculations and FE simulations. Temperature isotherms calculated from both approaches are also found to be in close agreement.

In machining at the low cutting speed, temperatures diffused deeper into the workpiece than machining at the higher cutting speed as it can be seen from Figs. 25–27. Higher temperature gradients should be expected in the workpiece for machining at

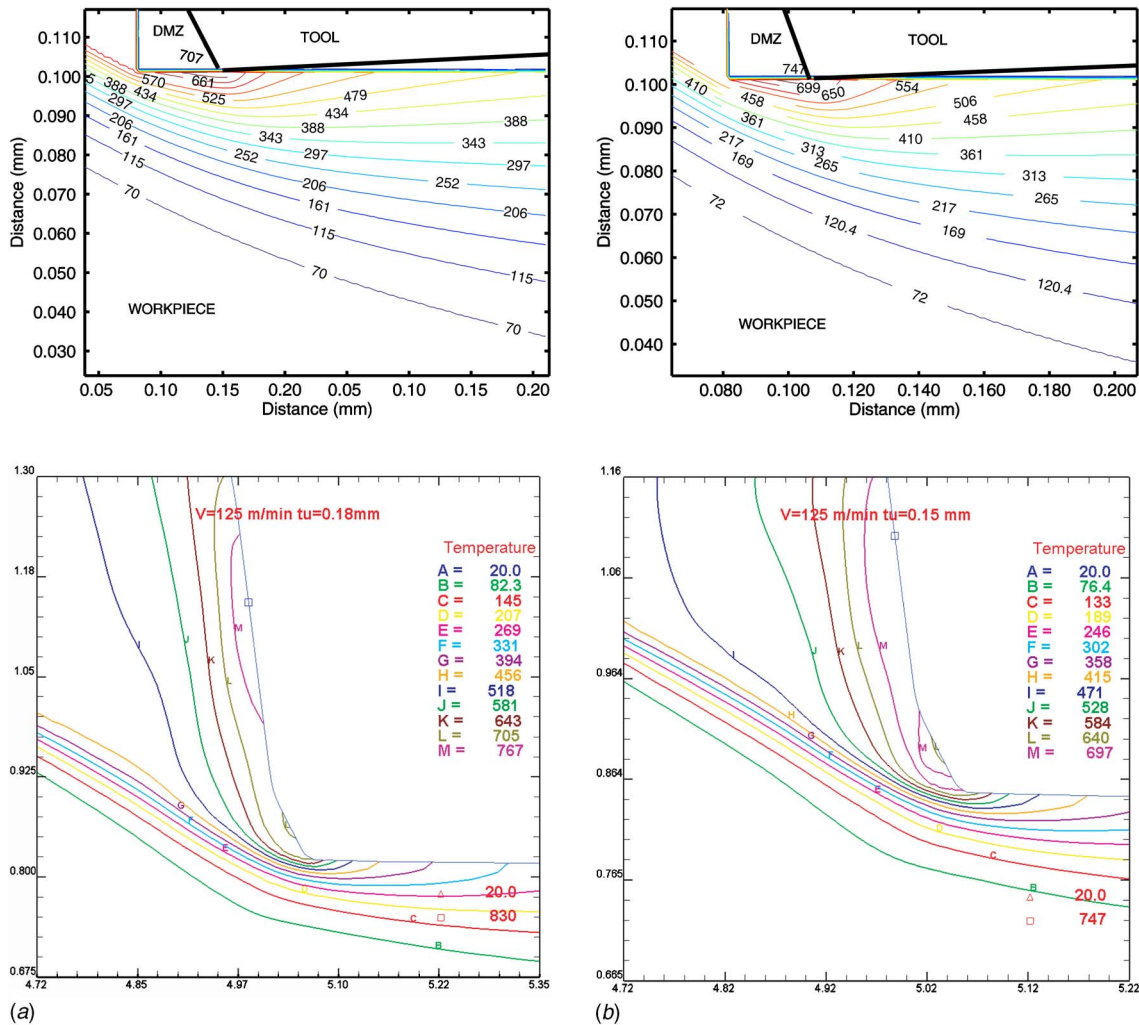


Fig. 27 Temperature distributions in the workpiece: (a) $V=125$ m/min, $t_u=0.18$ mm and (b) $V=125$ m/min, $t_u=0.15$ mm (all temperatures are in °C)

higher cutting speeds.

In the analytical thermal modeling approach, heat intensity at the primary shear zone is calculated from multiplying work material shear flow stress with shear velocity and frictional heat source under DMZ is calculated by multiplying shear flow stress with the friction factor under DMZ and velocity under DMZ (V_{AD}). It must be noted that due to the combined effect of these two heat sources, average temperature under DMZ (AD) is expected to be higher than average primary shear zone temperature (DE). Since the length AD is related to chamfer angle and chamfer height, higher temperatures might be expected at that zone with increasing chamfer angle. Higher temperatures will further soften the work material around DMZ. It should be noted that friction factors decrease with increasing cutting speed. In conjunction with decreasing friction factor under DMZ, lower heat intensities and lower temperatures may be generated in some cutting conditions. For instance, at the cutting speed of $V=175$ m/min, as uncut chip thickness increases average temperature under DMZ has decreased as shown in Fig. 28. However, average temperature under DMZ for the cutting speed of $V=125$ m/min has been found to increase with increasing uncut chip thickness.

8 Conclusions

In this study, mechanics of high-speed machining with chamfered tools is investigated. A slip-line field model is presented to explain material flow in the cutting zone during orthogonal cutting

with chamfered tools. The model considers that a dead metal zone is formed adjacent to the chamfer face of the tool edge during cutting. The slip-line angles and friction factors are identified by using experimental orthogonal cutting force data. An analytical thermal model for orthogonal cutting with chamfered tools is also introduced. The heat sources considered in this model are: (a)

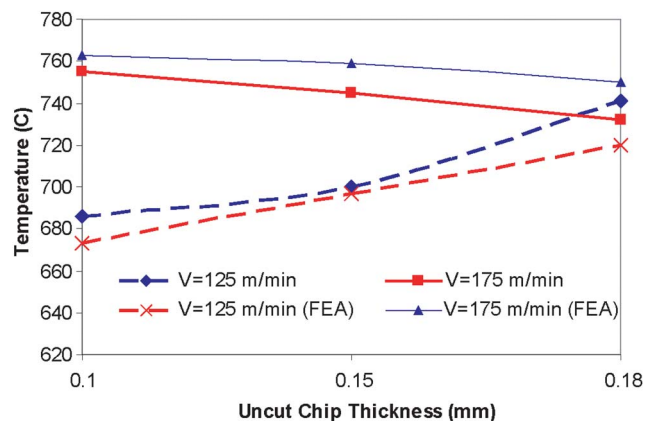


Fig. 28 Maximum temperatures under the dead metal zone T_{AD}

primary heat source due to shearing; (b) frictional heat source at the tool-chip interface; and (c) frictional heat source under DMZ. Intensities of these heat sources are calculated by utilizing slip-line field analysis. The temperature rises in the cutting tool and workpiece are computed and compared with finite element simulations. In addition, the influence of cutting conditions, i.e., cutting speed and uncut chip thickness on the temperature distributions along the chamfer and rake faces are explored.

The results indicate that a combined slip-line field analysis and analytical thermal modeling approach can be used in studying the influence of dead metal zone on the mechanics of high-speed cutting. According to the results given above, it is seen that the dead metal zone primarily affects the temperature distributions around the tip of the tool and eases the material flow due to thermal softening with increased temperatures. Since the size of the dead metal zone is mainly determined by chamfer angle, rake angle, and chamfer height, the selection of correct chamfered tool design for a given cutting process is important. Increasing chamfer angle will result in increased thrust forces and higher temperatures around DMZ which may reach a level of damage to the workpiece machined surface and high tool tip temperatures. These models can be utilized to design and optimize chamfered tools for high-speed machining of steels.

Nomenclature

A	= plastic equivalent strain in Johnson–Cook constitutive model (MPa)
a_i	= thermal diffusivity of the medium i
B	= strain related constant in Johnson–Cook constitutive model (MPa)
$B(x)$	= heat partition fraction
C	= strain-rate sensitivity constant in Johnson–Cook constitutive model
F_c, F_t	= cutting and thrust force components (N)
K_0	= zero order Bessel function of the second kind
k	= shear flow stress (N/mm ²)
m	= thermal softening parameter in Johnson–Cook constitutive model
m_1, m_2, m_3	= friction factors
n	= strain-hardening parameter in Johnson–Cook constitutive model
q	= heat intensity
T_M	= temperature rise (°C)
T_m	= melting temperature of the work material (°C)
t_u, t_c	= uncut and cut chip thickness (mm)
V, V_s, V_s, V_{ch}	= cutting velocity, shear velocity and chip velocity, (m/sec)
w	= width of cut (mm)
α	= dead metal zone angle (deg)
ϕ	= shear angle (deg)
τ	= frictional shear stress (N/mm ²)
λ	= thermal conductivity (W/m °C)
γ_1, γ_2	= rake and chamfer angle (deg)
$\zeta_1, \zeta_2, \zeta_3$	= slip-line angles (deg)
ρ	= prow angle (deg)
δ, θ	= slip-line central fan angles (deg)

References

- [1] Hitomi, K., 1961, "Fundamental Machinability Research in Japan," *J. Eng. Ind.*, **83**, pp. 531–544.
- [2] Kita, Y., Ido, M., and Kawasaki, N., 1982, "A Study of Metal Flow Ahead of Tool Face with Large Negative Rake Angle," *J. Eng. Ind.*, **104**, pp. 319–325.
- [3] Hirao, K., Tlustý, R., Sowerby, R., and Chandra, G., 1982, "Chip Formation with Chamfered Tools," *J. Eng. Ind.*, **104**, pp. 339–342.
- [4] Jacobson, S., and Wallen, P., 1988, "A New Classification System for Dead Zones in Metal Cutting," *Int. J. Mach. Tools Manuf.*, **28**, pp. 529–538.
- [5] Zhang, H. T., Liu, P. D., and Hu, R. S., 1991, "A Three-Zone Model and Solution of Shear Angle in Orthogonal Machining," *Wear*, **143**, pp. 29–43.

- [6] Ren, H., and Altintas, M. R., 2000, "Mechanics of Machining with Chamfered Tools," *ASME J. Manuf. Sci. Eng.*, **122**, pp. 650–659.
- [7] Oxley, P. L. B., 1989, *The Mechanics of Machining: An Analytical Approach to Assessing Machinability*, Ellis Horwood Limited, UK.
- [8] Movaheddy, M. R., Altintas, Y., and Gadala, M. S., 2002, "Numerical Analysis of Metal Cutting With Chamfered and Blunt Tools," *ASME J. Manuf. Sci. Eng.*, **124**, pp. 178–188.
- [9] Long, Y., and Huang, Y., 2005, "Force Modeling Under Dead Metal Zone Effect in Orthogonal Cutting with Chamfered Tools," *Trans. NAMRI/SME*, **33**, pp. 573–580.
- [10] Fang, N., 2005, "Tool-Chip Friction in Machining with a Large Negative Rake Angle Tool," *Wear*, **258**, pp. 890–897.
- [11] Lee, E. H., and Shaffer, B. W., 1951, "The Theory of Plasticity Applied to a Problem of Machining," *ASME J. Appl. Mech.*, **18**, pp. 405–413.
- [12] Fang, N., and Wu, Q., 2005, "The Effects of Chamfered and Honed Tool Edge Geometry in Machining of Three Aluminum Alloys," *Int. J. Mach. Tools Manuf.*, **45**, pp. 1178–1187.
- [13] Choudhury, I. A., See, N. L., and Zulkhairi, M., 2005, "Machining with Chamfered Tools," *J. Mater. Process. Technol.*, **170**, pp. 115–120.
- [14] Zhou, J. M., Walter, H., Andersson, M., and Stahl, J. E., 2003, "Effect of Chamfer Angle on Wear of PCBN cutting tool," *Int. J. Mach. Tools Manuf.*, **43**, pp. 301–305.
- [15] Yen, Y. C., Jain, A., and Altan, T., 2004, "A Finite Element Analysis of Orthogonal Machining Using Different Tool Edge Geometries," *J. Mater. Process. Technol.*, **146**, pp. 72–81.
- [16] Karpat, Y., and Özel, T., 2006, "Predictive Analytical and Thermal Modeling of Orthogonal Cutting Process. Part I: Predictions of Tool Forces, Stresses and Temperature Distributions," *ASME J. Manuf. Sci. Eng.* **128**(2), pp. 435–444.
- [17] Karpat, Y., and Özel, T., 2006, "Predictive Analytical and Thermal Modeling of Orthogonal Cutting Process. Part II: Effect of Tool Flank Wear On Tool Forces, Stresses and Temperature Distributions," *ASME J. Manuf. Sci. Eng.* **128**(2), pp. 445–453.
- [18] Karpat, Y., and Özel, T., 2006, "An Integrated Analytical Thermal Model for Orthogonal Cutting with Chamfered Tools," *Trans. NAMRI/SME*, **34**, pp. 9–16.
- [19] Hahn, R. S., 1951, "On the Temperature Developed at the Shear Plane in the Metal Cutting Process," *Proceedings 1st US National Congress of Applied Mechanics*, pp. 661–666.
- [20] Jaeger, J. C., 1942, "Moving Sources of Heat and the Temperatures at Sliding Contacts," *J. Proc. R. Soc. N. S. W.*, **76**, pp. 203–224.
- [21] Komanduri, R., and Hou, Z. B., 2000, "Thermal Modeling of Metal Cutting Process—Part I," *Int. J. Mech. Sci.*, **42**, pp. 1715–1752.
- [22] Komanduri, R., and Hou, Z. B., 2001, "Thermal Modeling of Metal Cutting Process—Part II," *Int. J. Mech. Sci.*, **43**, pp. 57–88.
- [23] Komanduri, R., and Hou, Z. B., 2001, "Thermal Modeling of Metal Cutting Process—Part III," *Int. J. Mech. Sci.*, **43**, pp. 89–107.
- [24] Ernst, H., and Merchant, M. E., 1941, "Chip Formation, Friction and High Quality Machined Surfaces," *Trans. ASME*, **29**, pp. 229–378.
- [25] Kudo, H., 1965, "Some New Slip Line Solutions for Two Dimensional Steady State," *Int. J. Mech. Sci.*, **7**, pp. 43–55.
- [26] Shi, T., and Ramalingam, S., 1991, "Slip Line Solution for Orthogonal Cutting with a Chip Breaker and Flank Wear," *Int. J. Mech. Sci.*, **33**(9), pp. 689–704.
- [27] Thomsen, E. G., McDonald, A. G., and Kobayashi, S., 1962, "Flank Friction Studies with Carbide Tools Reveal Sub-Layer Plastic Flow," *J. Eng. Ind.*, **84**, pp. 53–62.
- [28] Abebe, M., and Appl, F. C., 1981, "A Slip Line Solution For Negative Rake Angle Cutting," *Trans. NAMRI/SME*, **19**, pp. 341–348.
- [29] Waldorf, D. J., 1996, "Shearing, Ploughing and Wear in Orthogonal Machining," Ph.D. thesis, University of Illinois at Urbana-Champaign, Champaign, IL, 1996.
- [30] Fang, N., Jawahir, I. S., and Oxley, P. L. B., 2001, "A Universal Slip-Line Model with Non-Unique Solutions for Machining with Curled Chip Formation and a Restricted Contact Tool," *Int. J. Mech. Sci.*, **43**, pp. 557–580.
- [31] Fang, N., and Jawahir, I. S., 2002, "An Analytical Predictive Model and Experimental Validation for Machining with Grooved Tools Incorporating the Effects of Strains, Strain-Rates, and Temperatures," *CIRP Ann.*, **51**, pp. 83–86.
- [32] Childs, T. H. C., Maekawa, K., Obikawa, T., and Yamane, Y., 2000, *Metal Machining Theory and Applications*, Butterworth-Heinemann, London, UK.
- [33] Childs, T. H. C., 2006, "Numerical Experiments on the Influence of Material and Other Variables on Plane Strain Continuous Chip Formation in Metal Machining," *Int. J. Mech. Sci.*, **48**, pp. 307–322.
- [34] Carlslaw, H. S., and Jaeger, J. C., 1959, *Conduction of Heat in Solids*, Oxford University Press, Oxford, UK.
- [35] Johnson, G. R., and Cook, W. H., 1983, "A Constitutive Model and Data for Metals Subjected to Large Strains, High Strain Rates and High Temperatures," *Proceedings of the 7th International Symposium on Ballistics*, The Hague, The Netherlands, pp. 541–547.
- [36] Gray, G. T., Chen, S. R., Wright, W., and Lopez, M. F., 1994, "Constitutive Equations for Annealed Metals under Compression at High Strain Rates and High Temperatures," Los Alamos National Laboratory Report No. LA-12699-MS.
- [37] Cockroft, M. G., and Latham, D. J., 1966, A Simple Criterion of Fracture for Ductile Metals, National Engineering Laboratory, Report No. 216.